

## Loops in MY Lup?: Looking for asymmetries/substructures in an inclined protoplanetary disk

BAEZA, IAN                              

<sup>1</sup>*Institute of Astrophysics, Faculty of Exact Sciences, Universidad Andrés Bello, Santiago, Chile*

### ABSTRACT

The investigation of protoplanetary disks plays a crucial role in understanding the formation and evolution of planetary systems. The atmospheric properties and composition of mature exoplanets are ultimately determined by the composition and properties of their protoplanetary disks at the location of the planetary embryos, thus the physical/chemical history of the parent molecular clouds translates into the abundances to be found in exoplanets.

In this study, we analyze the protoplanetary disk MY Lup. We investigate the disk's structure and test it with simple theoretical models, utilizing data obtained from the Atacama Large Millimeter/submillimeter Array (ALMA), we use a multi-frequency analysis (ALMA Bands 6 and 7) to get a complete picture of the disk's features, both in the dust continuum and gas spectral lines.

We were able to reconstruct the images for the continuum and for 2 molecular lines, obtaining information of the kinematics of the disk, using this we run simple models assuming keplerian law and in this way we infer limits to the mass of the central star and we conclude that it's likely that a depletion of material is happening at 1.25 arcsec approx of offset form the center, and we suggest also the presence of radial drift phenomena.

*Keywords:* Protoplanetary Disk — YSOs — CO — ALMA

### 1. PROTOPLANETARY DISK

Protoplanetary disks are a crucial component in the development of Young Stellar Objects (YSOs). In the Fig (1) this process is schematized, the circumstellar disks originate shortly after the birth of YSOs (when a Molecular Cloud collapses and forms a core). As a result of the conservation of angular momentum, these cores give rise to circumstellar disks. Initially, these disks play a vital role in nourishing the star and facilitating successful accretion. However, as the star nears completion and progresses towards the main sequence, the residual material from this protostellar accretion disk forms what is known as a protoplanetary disk.[Dullemond & Monnier \(2010\)](#)

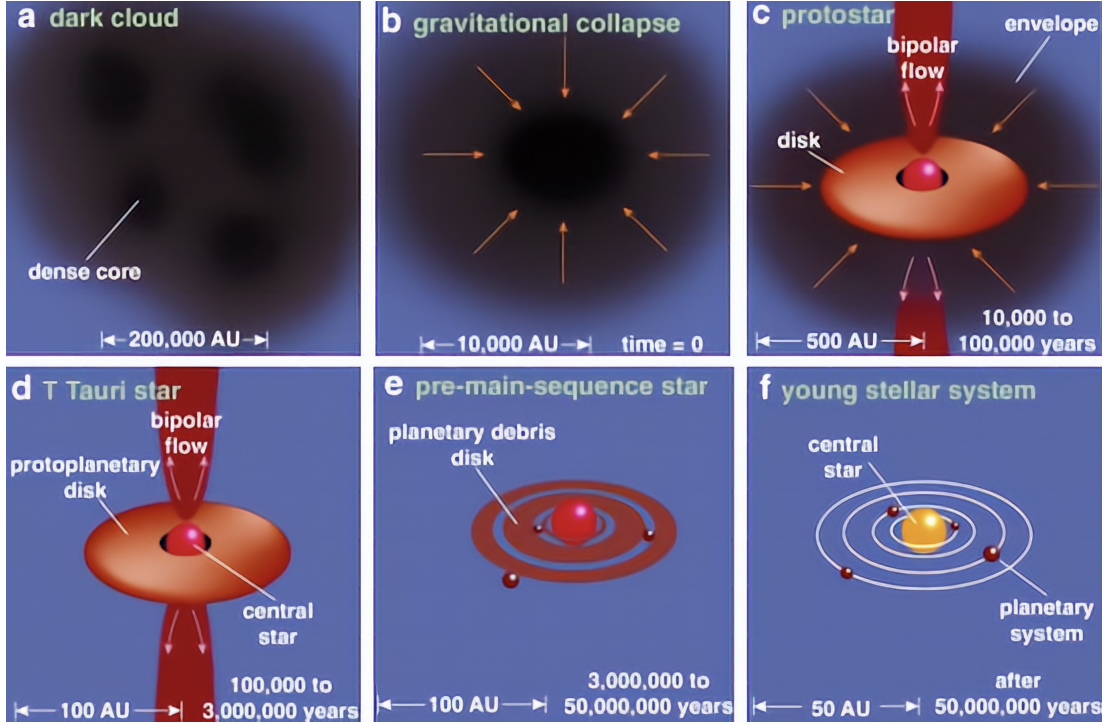


**Figure 1.** The early stages of a young star, similar to our Sun, can be explained through a series of phases that span over 50 million years. **a)** The process commences within dark interstellar clouds that contain areas with high density. **b)** These dense regions become unstable due to gravity and collapse under their own weight. **c)** This collapse initiates the formation of a protostar, which is a stage in the star's evolution characterized by rapid mass accumulation from a surrounding disk of material. **d)** At this point, the protostar is encompassed by a cloud of gas and dust. As this dusty envelope disperses, the protostar becomes visible for the first time in optical wavelengths, taking on the appearance of a T Tauri star. **e)** After millions of years, the dusty disk dissipates, leaving behind a pre-main-sequence star at the center. In some instances, a debris disk may continue to orbit the star, consisting of newly formed planets. **f)** Eventually, the star undergoes gravitational collapse until its core temperature reaches a level at which nuclear fusion can occur, resulting in the star becoming a main-sequence star. (Figure taken from Greene (2001)).

A classification has emerged for the Protoplanetary disk's in the mid 80's and refined in the 90's based on the slope of the spectral energy distribution (SED) between about 2 and 25  $\mu\text{m}$  where the spectral index is defined as follows,

$$\alpha_{IR} = \frac{d \log (\nu F_\nu)}{d \log (\nu)} = \frac{d \log (\lambda F_\lambda)}{d \log (\lambda)} \quad (1)$$

This index leads to four classes, 0-I-II-III, that have a correlation with the evolutionary stages in previously mentioned, where panel **c**) in Fig (1) will correspond to the Class 0 in Fig (2), this class is dominated by the envelope around the protostar (it means that it is still optically thick), the Class I corresponds to the transition of panel **c**) to **d**) that happens when the envelope becomes optically thin, Class II is directly related with the panel **d**) and it is achieved when the envelope is completely removed, finally the Class III corresponds to **e**) panel and becomes harder to detect

the contribution of the disk. It is worth to mention that this definition have some degeneracy since due inclination with respect to our line of sight of the disk could generate extinction and this being miss-interpreted as a younger Class. [Williams & Cieza \(2011\)](#)

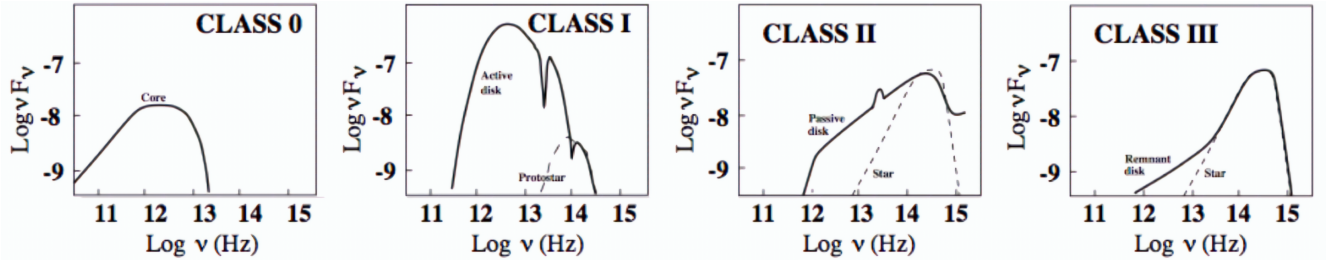


**Figure 2.** Evolution of Disk Classes based on Spectral Index. These classes has a correspondence with the evolution. In Class 0, a central core deeply embedded within a larger envelope accumulates material. Progressing to Class I, the central core gains mass, accompanied by the formation of a flat accretion disk around it. Class II objects predominantly feature a disk composed of gas and dust, containing most of the material surrounding the star. Lastly, Class III objects exhibit minimal disk emissions, closely resembling the SED of a typical star. (Modified figure from [Isella \(2006\)](#))

In this context some protoplanetary discs exhibit characteristics such as inner holes and gaps, which have been detected through millimetre interferometric observation (e.g. [Andrews et al. \(2018\)](#); [Huang et al. \(2018a,b\)](#)), and in infrared (e.g [Avenhaus et al. \(2018\)](#)), different sub-structures could appear due several physical mechanisms (see Fig (3) and [Andrews \(2020\)](#) for a detailed description). Observations indicates that substructures are widespread and play a significant role in various processes related to the evolution of disks and the formation of planets (e.g [Huang et al. \(2018a,b\)](#)). This presents a great opportunity as precise measurements of millimeter continuum can provide valuable information on the types, frequency, and variations of these substructures within disks. Understanding these substructures can contribute to the development of a stronger theoretical understanding of the early stages of planetary system formation.

In this work we re-address this search of structures for the T-tauri star MY Lup, using data form ALMA we look for asymmetries in the disk around the star, and retrieve some limits for intrinsic parameters of the system.

## 2. DATA AND TARGET

### 2.1. *MY Lup*

MY Lup is a T Tauri star ([Gregorio-Hetem et al. 1992](#)), is located in the Lupus IV cloud is a K0-type star with a mass estimated around of  $1.23 M_{\odot}$ , and is surrounded by a highly inclined ( $\sim 70^\circ$ ) disk ([Comerón 2008](#); [Andrews et al. 2018](#)) and is situated at a distance of  $157.15 \pm 0.89 pc$  ([Gaia Collaboration et al. 2023](#)). From multi band spectroscopy measurements [Romero et al. \(2012\)](#) proposed that its SED could be

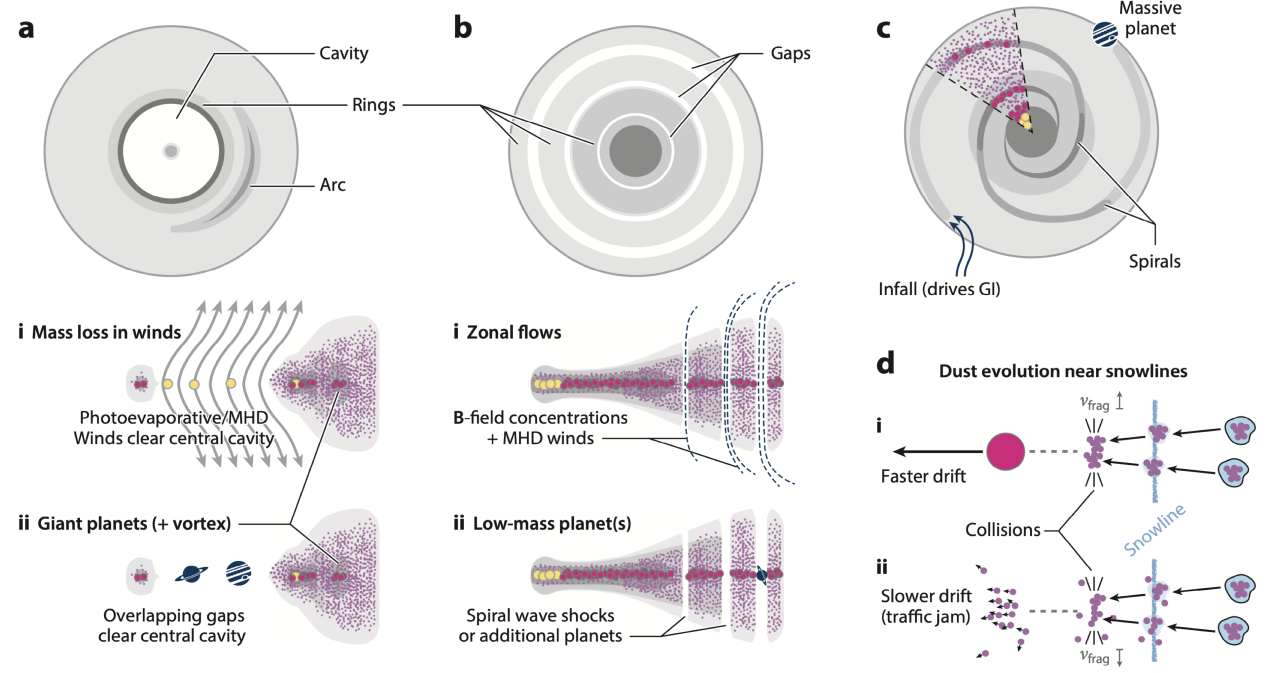


**Figure 3.** Schematic illustrations of the substructures generated by various physical mechanisms. Grayscale denotes gas densities ( $\propto P$ ) and representative solid densities are marked with exaggerated symbol sizes and colors. (a) A schematic of a ring–cavity substructure morphology with a pronounced arc feature generated by a vortex. The two side views represent the behavior for a disk with substantial mass loss in a photoevaporative or MHD-driven wind (a, i) or a series of giant planets (a, ii), both of which effectively diminish  $\Sigma_g$  in a central cavity. The sharp density contrast at the cavity edge can trap particles in a ring and potentially generate a vortex. (b) A schematic of the ring–gap substructure morphology, with similar behavior produced by the magnetic field concentrations inherent in MHD zonal flows (b, i) and the perturbations from interactions between lower-mass planets and a relatively inviscid disk (b, ii). (c) A simplified diagram of the spiral wave perturbations that could be produced by the global GI driven by remnant envelope infall or tidal interactions with a massive (external) planetary companion. (d) A diagram highlighting two representative outcomes for the evolution of icy aggregates as they migrate across a volatile condensation front. Subpanel i shows the case in which ice loss due to sublimation enhances  $v_{frag}$ , and thereby promotes growth and drift; subpanel ii shows the opposite, resulting in a pileup of small, bare grains. Abbreviations: GI, gravitational instability; MHD, magnetohydrodynamics. (Figure and Caption from Andrews (2020))

explained by a discontinuity in the grain size distribution rather than an inner opacity hole. A couple of years later Avenhaus et al. (2018), using the SPHERE instrument, confirmed a high inclination of  $\sim 77^\circ$  of the dusty disk, also revealed a flared-truncated disc structure with multiple but not clear rings on the surface. The Disk Substructures at High Angular Resolution Project (DSHARP; Andrews et al. (2018)) detected faint annular substructures at 8, 20, 30, and 40au from the central star (Huang et al. 2018a), without any indication of a large inner cavity.

Due to the inclination of the disk and likely due to extinction it's hard to obtain a reliable estimation of age (as mentioned in Alcalá et al. (2019)) was previously estimated an age of approximately 16.6 Myr (Frasca et al. 2017), while Andrews et al. (2018)

suggested an age around 10 Myr and more recently Long et al. (2022) has estimated the age around 2 Myr considering this effect of reddening.

## 2.2. ALMA Data

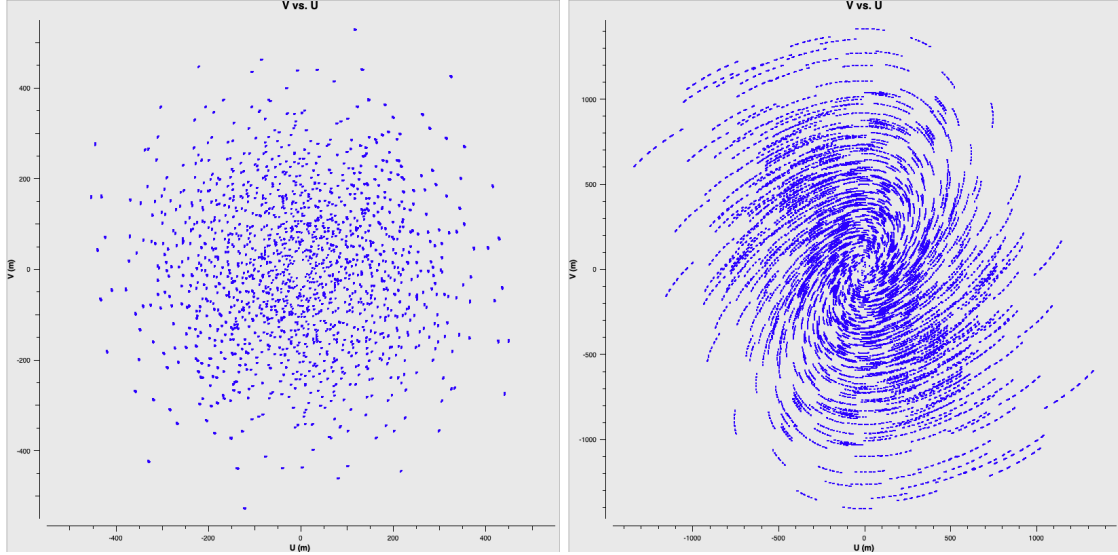


**Figure 4.** UV coverage for Band 6 spw 0, and Band 7 spw 3 respectively (see tables 1,2 for details). From this image we can clearly see that we have a better coverage for the Band 7 spw 3, this impacted in our decision in the analysis of base more in this line of emission (see text below).

MY Lup was observed with ALMA in band-6 and band-7 with two different configurations during Cycle-2 (programme 2013.1.00663.S, PI: Canovas).

In Band 6, 40 (12-m) antennas were used during the observations with baselines ranging from 23.3 to 558.2 m (17.9 to 429.4  $k\lambda$ , see Fig (4) left panel). The ALMA correlator was configured to provide one continuum spectral window with a total bandwidth of 2 GHz centred at 231.6 GHz and three spectral windows with bandwidths of 58.6 MHz and channel widths of 61.035 KHz. These narrow windows were centred on the  $^{12}CO$  (2-1, 230.5 GHz) (hereafter 12CO),  $^{13}CO$  (2-1, 220.4 GHz), and  $C^{18}O$  (2-1, 230.5 GHz) lines.

The Band 7 observations were performed with 42 (12-m) antennas with baselines ranging from 15.1 to 1574.4 m (17.3 to 1789.1  $k\lambda$ , see Fig (4) right panel). The correlator was configured to provide two continuum spectral windows with a total bandwidth of 2 GHz centred at 332.5 and 343.7 GHz, and two spectral windows with bandwidths of 58.6 MHz and channel widths of 61.035 KHz aimed to measure the  $^{12}CO$  (3-2, 345.8 GHz) and  $^{13}CO$  (3-2, 330.6 GHz).

The quasars QSO J1517-2422 and QSO J1610-3958 were observed for bandpass and phase calibration. Titan and Ceres were observed to perform flux calibration in Band 6 and Band 7, respectively. (The last fourth paragraphs were obtained from Canovas et al. (2016) which is the paper associated with these observations).

The handling of visibility's was done with the software CASA ([CASA Team et al. 2022](#)) in the process of getting images, and a process of self calibration was done in order to increase the signal to noise ratio. (For further details on data reduction, the interested reader is referred to the Appendix A)

### 3. ANALYSIS

#### 3.1. Continuum

From each Band we have selected all channels that were not part of any emission line or the edges of the spectral window, first we have analysed directly the visibility's with the software Frank ([Jennings et al. 2020](#)), which fits a Gaussian's to the azimuthally averaged profile (a single radial profile) in order to get the shift from the center (dRa and dDec), the position angle (PA) and the inclination (i) of the disk (also this allow us to see if we have cavities or depletion of material).

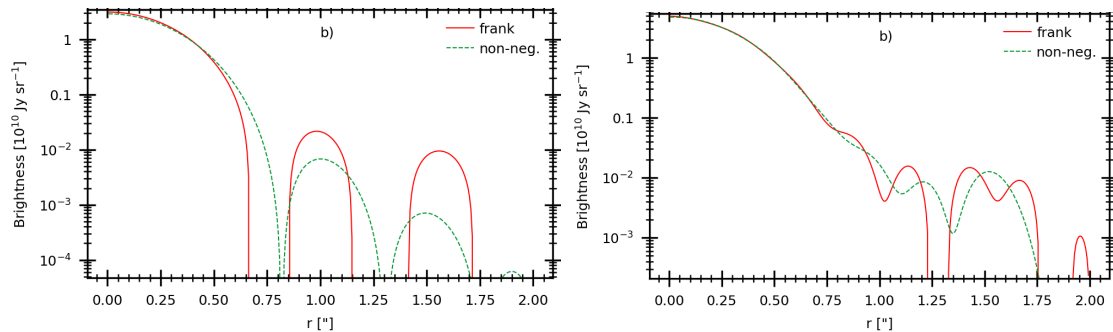


**Figure 5.** Deprojected and azimuthally averaged radial intensity, for all continuum in Band 6 and 7 respectively

We have test this by different calibrations but generates the same pattern (see Fig (5)) as long as we use the same binning in time and channels, for Band 6 we used a channel binning of 20 and a time average of "150s", while for the Band 7 we have used also a 20 channels of binning but "90s" in the time average (this is need in order to reduce the size of the uvtables which were obtained with the software UVplot ([Tazzari 2017](#)) a tool that can be installed and used inside CASA that read the tables and generates txt files with the visibility's., and our experiments have shown that depending of this binning we can appreciate different results).

For each Band we were able to reconstruct the images using tclean task from CASA (after the self calibration process, see Appendix A) shown in Fig (6). It is clear that we have much higher resolution on the Band 7, hence most of our analysis is based on this Band and then extended when is possible to the other.

For the Band 7 we have also deprojected this image in order the radial profile and contrast with the previous results obtained from the Frank software this can be seen in Fig (7), this step must be take with caution since for some reason the Position angle in the figures were shifted by around 10 degrees with respect to our results from frank and from the literature (e.g. [Huang et al. \(2018a\)](#)).

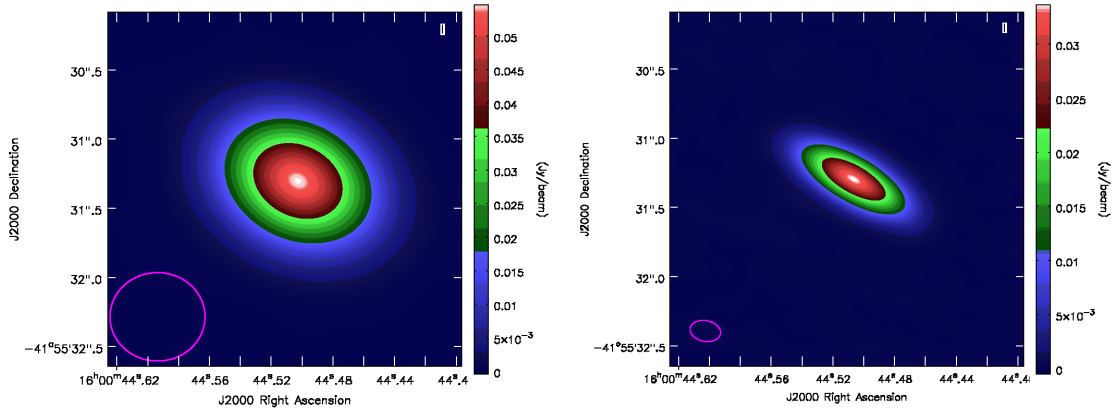


**Figure 6.** We are showing the continuum along the whole band and the resulted image interpolated for viewing purpose (bicubic), also is plotted the beam size and the typical area in pixels are around 5 pixels<sup>2</sup>/beam .**Left:** Band 6 **Right:** Band 7.

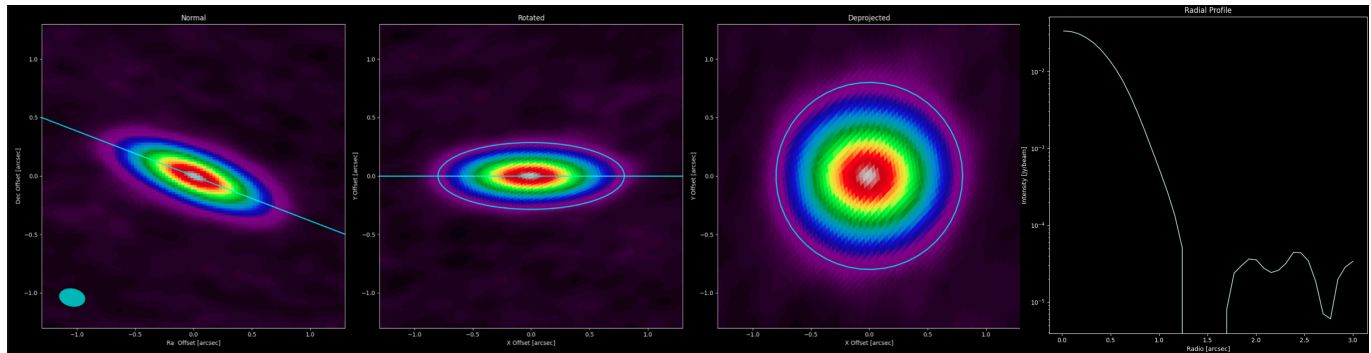


**Figure 7.** Deprojection performed to the continuum image of the Band 7

But even considering that we can consider that the same decrement occurs around 1.25 arcseconds which is consistent with the obtained result from Frank (see Fig (5) right Panel).

### 3.2. Lines

For the lines we subtract the continuum with the task UVcontsub from CASA and use tclean to reconstruct the images per channel (for details see Appendix A), unfortunately due the low signal to noise in most of the lines we just consider two lines for our analysis , Band 6 spectral window 0 ( $^{13}CO_{(J=2-1)}^{(v=0)}$ ) and Band 7 spectral window 3 ( $CO_{(J=3-2)}^{(v=0)}$ ).

For those lines we compute their integrated intensity over the spectral line, the intensity-weighted velocity of the spectral line and the velocity dispersion of the spectral line (here after Moment 0, Moment 1 and Moment 2, respectively). We compute these moments making use of the tool BetterMoments (Teague & Foreman-Mackey 2018) and can be found on Fig (8), from these images is easy to visualise the rotation of the disk and that it behaves as we expect.

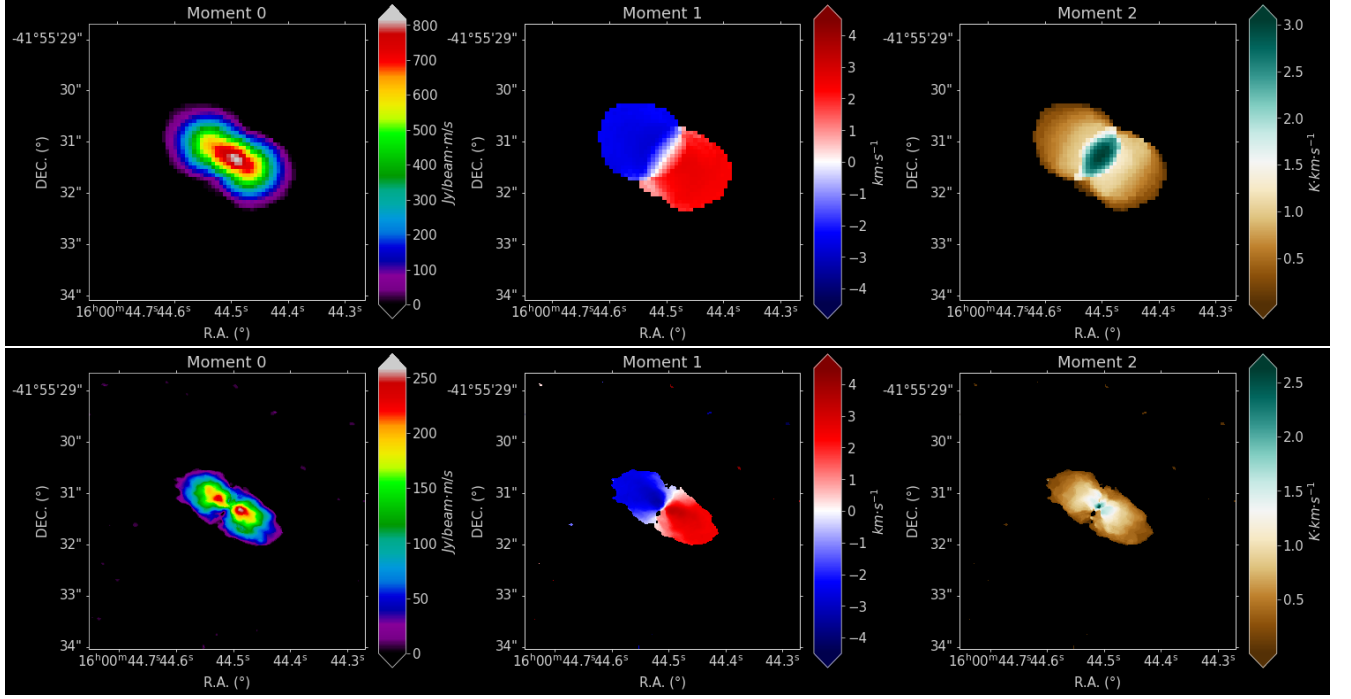


**Figure 8.**

**Top Row:** Moment maps (0,1,2) for  $^{13}CO_{(J=2-1)}^{(v=0)}$  line (Band 6 spw 0).

**Bottom Row:** Moment maps (0,1,2) for  $CO_{(J=3-2)}^{(v=0)}$  line (Band 7 spw 3)

We have tried to model these maps in order to obtain physical properties of the system (such as the mass of the central star, extension in height, radius, etc) but the models for some reason did not converge properly so we decide to not attempt further in this kind of analysis, we suspect that this may be caused by two factor, first as can be see more clearly in the moment 0 of band 7 spw 3 (Bottom panel Fig (8)), we were not able to recover the flux in the middle of the disk this may be cause due the there's material from the cloud in larger scales at the same frequency hence the deconvolver is not able to recover this flux since are part of an structure in much larger scale (this effect can also be seen in Fig (10)), the other factor that may be causing troubles at the time constrain the models is that likely these lines are partially optically thick and due this we are not able to see the innermost part of the disk were these simple models are tightly dependant.

On the other hand we have tried another approach studying the PV diagrams along the major axis of the disk in a very narrow line (about 3 pixels of width), to perform the analysis we have used SLAM (Aso & Sai 2023), a tool which maps points according to the edge and ridge on slices of the diagram and those point are fitted with single (or double) power law. We perform our PV diagrams for our Band 7 spw 3 and Band 6 spw 0 spectral lines using CASA with the imview task, we use the value of Position Angle derived form Frank in and the contour of the moment maps to guide us in the process of generate the line (since the parameter can not be inputted by hand), in Fig

(9) can be seen the our PV diagrams for our lines in band 6 and 7 and also plotted the contours and point found with SLAM.

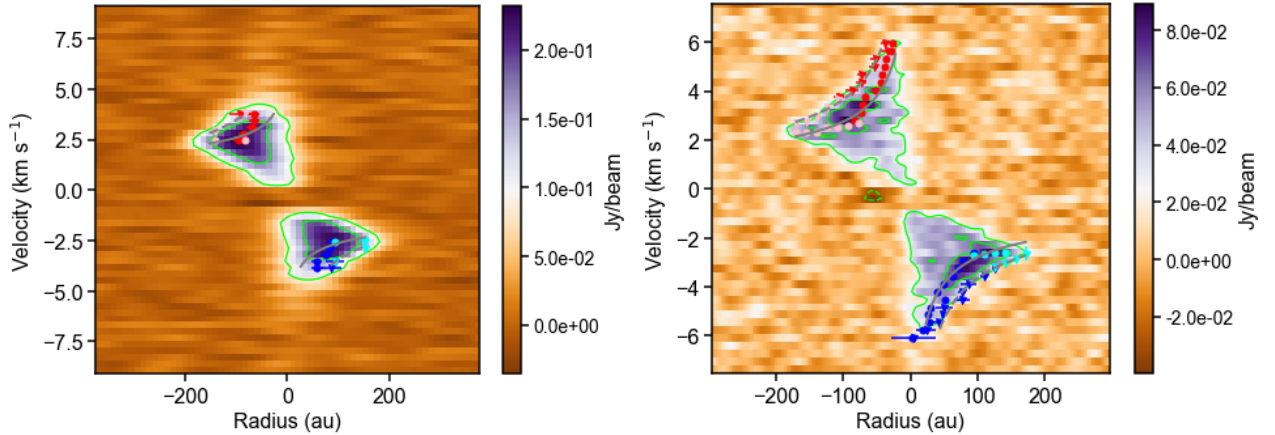


**Figure 9.** PV diagrams for line  $^{13}CO_{(J=2-1)}^{(v=0)}$  and  $CO_{(J=3-2)}^{(v=0)}$  respectively, also are plotted the contours and point found and fitted by SLAM

With this approach we were able to infer some values/properties of the system that will be discussed in the next section, (the complete output can is briefly described and shown in Appendix B).

#### 4. RESULTS AND DISCUSSION

In the previous section we describe several software used to determine different properties of the disk, presented here in the same order that were presented before.

From Frank (Jennings et al. 2020) we retrieve from the continuum the shift from the center  $dRA : -0.05 \pm 0.032$  arcsec  $dDec : +0.03 \pm 0.025$  arcsec , an inclination  $i = 70.02 \pm 3.07$  deg and a position angle of  $PA = 59.4 \pm 1.8$  deg ,these values are the mean of the all outputs (since we have tested considering different calibrations) and the errors are the simple standard deviation of these values. Also these values are in relly good agreement with previous estimations (e.g Huang et al. (2018a)).

From this step also we suggest that as Romero et al. (2012) there's a presence of the phenomena of Radial drift, this came out from the difference in the first decrement of brightness in the radial profiles, that at least for the Band 7 also can be cross checked from the radial profile acquired from the deprojection of the image (even if these step require be checked in the near future).

Using the Moment Maps we can infer that the flux of the rest frequency material is lost due "missing short-spacing" so the interferometer is not able to resolve the flux of the rest frequency due is become part of the flux of the whole cloud which is a large scale structure and the shorter base line available are not able to recover their measures. (Also can be seen in the spectral profiles in Fig Fig (10) in the Appendix). Moreover we can constrain also the rotation velocity of the disk around  $\sim 4.5$  km/s (also reaffirm the system velocity of 4.37 km/s), furthermore form the moment 2 we

can notice that the movement of the gas becomes more coherent as approach to the center (these is consistent with what we found from SLAM, see below).

Finally from SLAM ([Aso & Sai 2023](#)), we were able to delimitate a range of mass of the central T tauri star about  $[0.879 \pm 0.02, 1.686 \pm 0.06] M_{\odot}$  and a radius range of  $[61.68 \pm 0.83, 94.6 \pm 1.79] AU$ , this values comes from the analysis of the ridge and edge point fitted by SLAM respectively, also here we report the values obtained from the  $CO_{(J=3-2)}^{(v=0)}$  line since the line of  $^{13}CO_{(J=2-1)}^{(v=0)}$  even if converged properly had return a much wide range. The fit of slam suggest that only one power law is needed to reproduce the behaviour of this disk following values near to the keplerian rotation ( $velocity \propto \frac{1}{r} .5$ ). These results are also in good agreement with previous estimations (e.g. ([Huang et al. 2018a](#); [Alcalá et al. 2019](#))).

Futures works could address the values that we have estimated here, a practical approach could be include more data from another wavelengths/techniques or more measurements form ALMA in order to combine them and obtain better signal to noise for all the lines.

## 5. ACKNOWLEDGMENTS

- <sup>1</sup> I would like to thank to Professor Claudio Caceres. for your time and the patient
- <sup>2</sup> to teach me the useful tools and knowledge about ALMA data treatment and proto-
- <sup>3</sup> planetary disks along this practical course.

*Facilities:* ALMA

*Software:* Astropy ([Astropy Collaboration et al. 2013, 2018](#)), Numpy ([Harris et al. 2020](#)), Matplotlib ([Hunter 2007](#)), Scikit-learn ([Pedregosa et al. 2011](#)), CASA ([CASA Team et al. 2022](#)), UVplot [Tazzari \(2017\)](#), Frank Jennings et al. ([2020](#)), SLAM [Aso & Sai \(2023\)](#).

## APPENDIX

### A. DATA REDUCTION INFORMATION

#### A.1. *Self Calibration*

Self Calibration<sup>1</sup> process was include in order to get higher signal to noise, we applied 4 solutions to each Band, having a large and a short solution for Phase and Amplitude in this order, in specific for Band 7 we have applied solution intervals of "inf" , "96s" , "180s" and "108s" in the order mentioned and for the Band 6 "120s", "72s", "inf" and "84s" respectively.

From this process we obtain the images from the continuum.

#### A.2. *Handling ALMA data*

Here I briefly describe the process that we perform to obtain the lines images.

After the self calibration the we create a dirty cube in order to see what we have in our hands, after carefully selected the bands of continuum (done in the previous step with the Fig (10)) , we use the task constsub of CASA to subtract the continuum after this we create several images varying the parameters of weightings of the baselines with the task tclean of CASA, Finally we decide to use the Natural weighting in order to retrieve the higher possible amount of flux.

##### A.2.1. *Band 6*

Summarized is the origin info of Band 6 and 7 in tables 1 and 2 respectively. For testing which binning can be use and see general information of the data we created "dirty" cubes with all the spectral channels available. From Fig (10), we decide the channels to include as continuum or lines also which channels discard (e.g. Band 7 spw 3 the last channel), furthermore even if we tried this images can let us know from which band we were able to reconstruct useful images.

For Band 6 we use 512 pixel and a pixel size of 0.15 arcsec for the dirty images, while for the clean figures we use 1024 pixels and a pixel size of 0.075 arcsec (roughly 5 pixels inside of the minor axis of the beam).

We defined the continuum as follows (in notation that CASA reads, used in task contsub)

```
continuum =0 : 10 ~ 305; 590 ~ 949
          1 : 10 ~ 109
          2 : 10 ~ 370; 650 ~ 949
          3 : 10 ~ 385; 640 ~ 949
```

<sup>1</sup> To perform self calibration I based my analysis on the procedure and codes from I-Train  
<https://almascience.eso.org/tools/eu-arc-network/i-train>

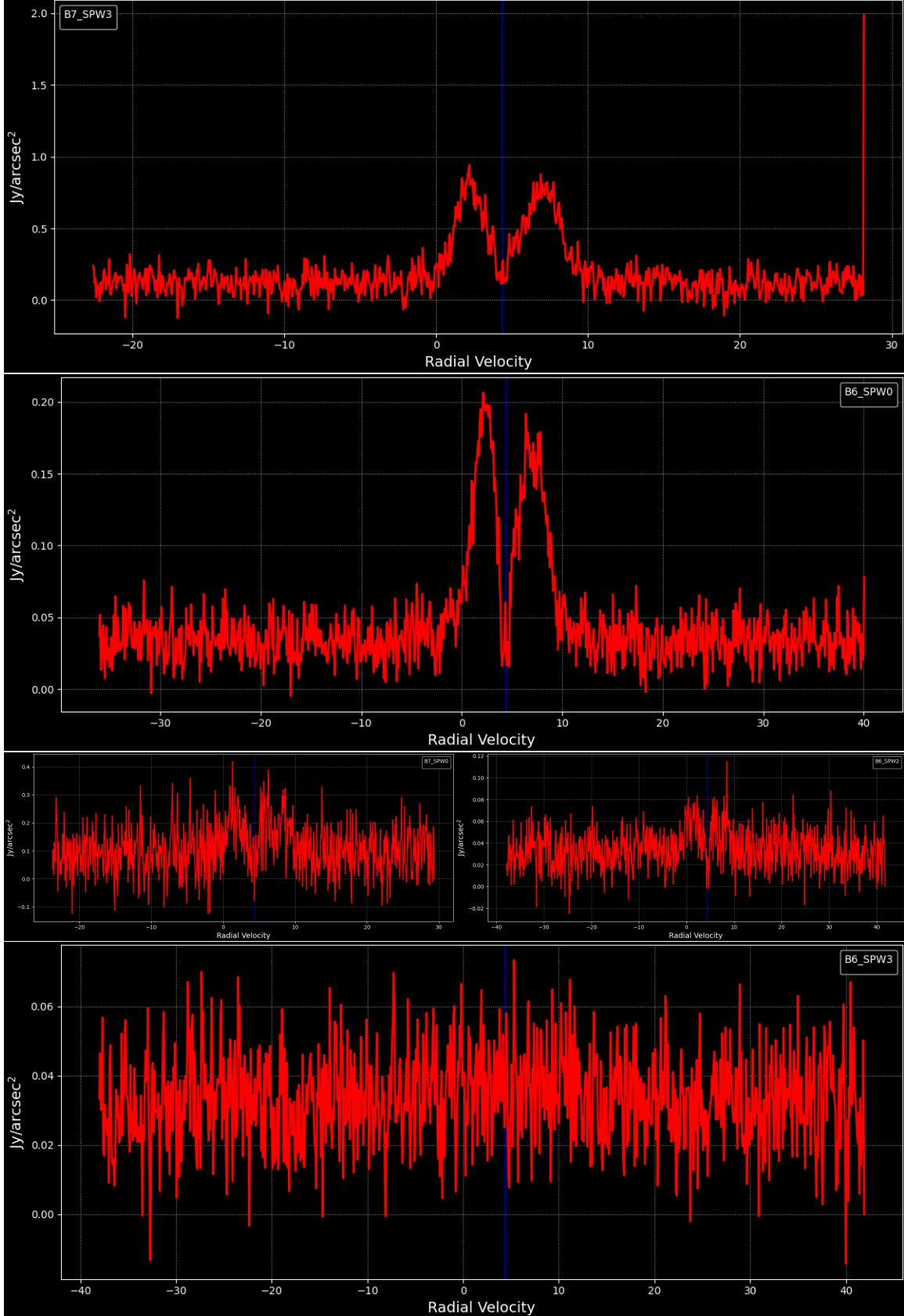


**Figure 10.** Mean flux along the spectral axis of the cubes inside of a polygon surrounding the emission, the blue lines represent the system velocity (4.37 km/s), these images were used to determine binning of channel , areas were the lines were placed and if the central velocity was properly attributed. Moreover from these images we can see that we lost most of the flux on the rest velocity as discussed before we suggest that this is due "short-spacing problem"

For lines we have used (spw:[nchan,start,width,reffreq])

<i>DATA</i> =0 :	[61	-9.84188km/s	0.31748km/s	230534.6396MHz]
	2 : [35	-11.95515202km/s	0.664175112km/s	220395.4716MHz]
	3 : [61	-10.33416km/s	0.33336km/s	219557.1576MHz]

**Table 1.** The table show information of the Band 6 Data.

Band 6	Rest Frequency	Central Frequency <sup>a</sup>	Chanel width	Frames	Target Line <sup>b</sup>
spwid	MHz	MHz	kHz		
0	230538.0000	230534.6396	-61.035	960	$^{13}CO_{(J=2-1)}^{(v=0)}$
1	231600.0000	231596.6241	15625	128	Continuum
2	220398.6842	220395.4716	61.035	960	$^{13}CO_{(J=2-1)}^{(v=0)}$
3	219560.3580	219557.1576	61.035	960	$C^{18}O_{(J=2-1)}^{(v=0)}$

<sup>a</sup> this implies a system velocity of 4.37 km/s

<sup>b</sup> this lines where associated based in the rest frequency line to the [splatalogue catalogue](#)

### A.2.2. Band 7

For Band 7 we use 512 pixel and a pixel size of 0.08 arcsec for the dirty images, while for the clean figures we use 2048 pixels and a pixel size of 0.02 arcsec (roughly 5 pixels inside of the minor axis of the beam).

We defined the continuum as follows (in notation that CASA reads, used in task contsub)

<i>continuum</i> =0 :	20 350; 690 949
	1 : 1 : 10 109
	2 : 10 109
	3 : 10 290; 600 949

For lines we have used (spw:[nchan,start,width,reffreq])

<i>DATA</i> =0 :	[71	-11.9556km/s	0.3321km/s	330583.1465MHz]
	3 : [51	-8.25552km/s	0.31752km/s	345790.9495MHz]

**Table 2.** The table show information about Band 7.

Band 7	Rest Frequency	Central Frequency <sup>a</sup>	Chanel width	Frames	Target Line <sup>b</sup>
spw_id	MHz	MHz	kHz		
0	330587.9653	330583.1465	-61.035	960	$^{13}CO_{(J=3-2)}^{(v=0)}$
1	331600	331595.1664	-15625	128	Continuum
2	344800	344794.9740	15625	128	Continuum
3	345795.99	345790.9495	61.035	960	$CO_{(J=3-2)}^{(v=0)}$

<sup>a</sup> this implies a system velocity of 4.37 km/s

<sup>b</sup> this lines where associated based in the rest frequency line to the [splatalogue catalogue](#)

## B. OUTPUTS OF SLAM

Here we show all the outputs that were not showed in the paper of SLAM for the Band 7 spw 3 (since is from were we report results), fro figure 11 we can see that the edge and ridge points are being properly founded in the distributions, this also is being reflected after in the MCMC that hdd been run in order to fit the power law (see Fig (12)). Finally another perspective of the PV diagram is shown in figure 13 where we can appreciate more easily how good the estimation of the points it's done, all this complementary material is just to reinforce that we can trust in our results.

## REFERENCES

- Alcalá, J. M., Manara, C. F., France, K., et al. 2019, A&A, 629, A108, doi: [10.1051/0004-6361/201935657](https://doi.org/10.1051/0004-6361/201935657)
- Andrews, S. M. 2020, ARA&A, 58, 483, doi: [10.1146/annurev-astro-031220-010302](https://doi.org/10.1146/annurev-astro-031220-010302)
- Andrews, S. M., Huang, J., Pérez, L. M., et al. 2018, ApJL, 869, L41, doi: [10.3847/2041-8213/aaf741](https://doi.org/10.3847/2041-8213/aaf741)
- Aso, Y., & Sai, J. 2023, arXiv e-prints, arXiv:2311.07988, doi: [10.48550/arXiv.2311.07988](https://doi.org/10.48550/arXiv.2311.07988)
- Astropy Collaboration, Robitaille, T. P., Tollerud, E. J., et al. 2013, A&A, 558, A33, doi: [10.1051/0004-6361/201322068](https://doi.org/10.1051/0004-6361/201322068)
- Astropy Collaboration, Price-Whelan, A. M., Sipőcz, B. M., et al. 2018, AJ, 156, 123, doi: [10.3847/1538-3881/aabc4f](https://doi.org/10.3847/1538-3881/aabc4f)
- Avenhaus, H., Quanz, S. P., Garufi, A., et al. 2018, ApJ, 863, 44, doi: [10.3847/1538-4357/aab846](https://doi.org/10.3847/1538-4357/aab846)
- Canovas, H., Caceres, C., Schreiber, M. R., et al. 2016, MNRAS, 458, L29, doi: [10.1093/mnrasl/slw006](https://doi.org/10.1093/mnrasl/slw006)
- CASA Team, Bean, B., Bhatnagar, S., et al. 2022, PASP, 134, 114501, doi: [10.1088/1538-3873/ac9642](https://doi.org/10.1088/1538-3873/ac9642)
- Comerón, F. 2008, in Handbook of Star Forming Regions, Volume II, ed. B. Reipurth, Vol. 5 (ESO), 295
- Dullemond, C. P., & Monnier, J. D. 2010, ARA&A, 48, 205, doi: [10.1146/annurev-astro-081309-130932](https://doi.org/10.1146/annurev-astro-081309-130932)
- Frasca, A., Biazzo, K., Alcalá, J. M., et al. 2017, A&A, 602, A33, doi: [10.1051/0004-6361/201630108](https://doi.org/10.1051/0004-6361/201630108)
- Gaia Collaboration, Vallenari, A., Brown, A. G. A., et al. 2023, A&A, 674, A1, doi: [10.1051/0004-6361/202243940](https://doi.org/10.1051/0004-6361/202243940)
- Greene, T. 2001, "Stellar embryology" takes a step forward with the first detailed look at the youngest Sun-like stars. <https://www.americanscientist.org/article/protostars>

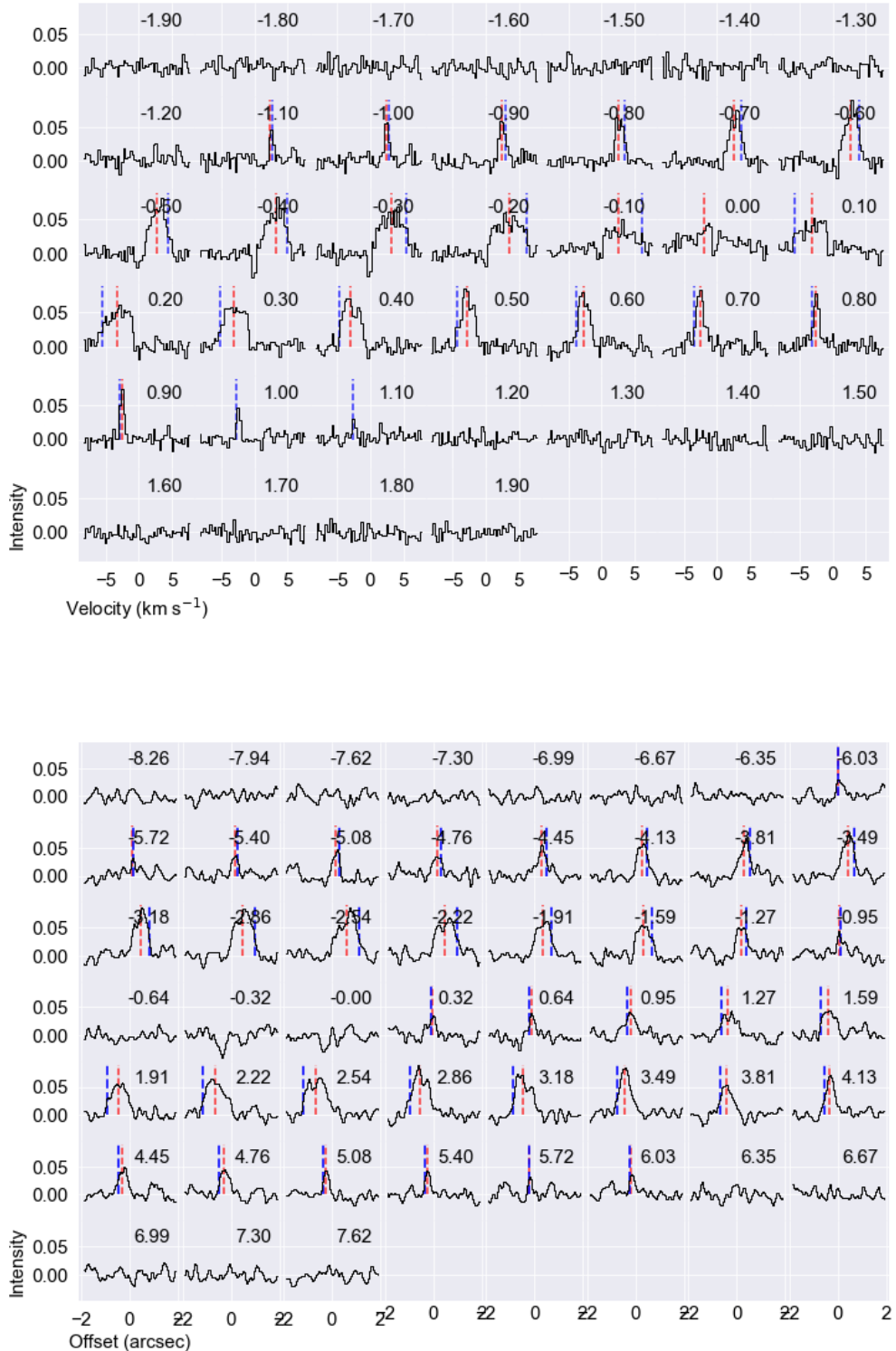


**Figure 11.** X and V cuts of slam for Band 7 spw 3 where we can see that the edge and ridge fits properly the distributions

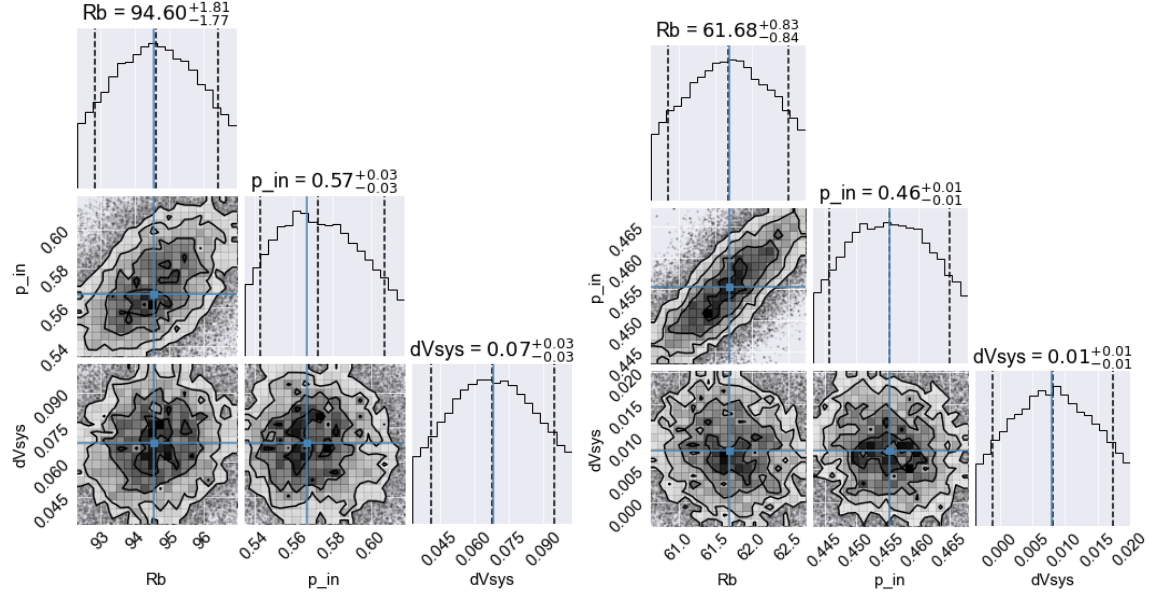


**Figure 12.** Corner plots of the convergence of the points found in the PV diagram of Band 7 spw 3 for edge and ridge respectively

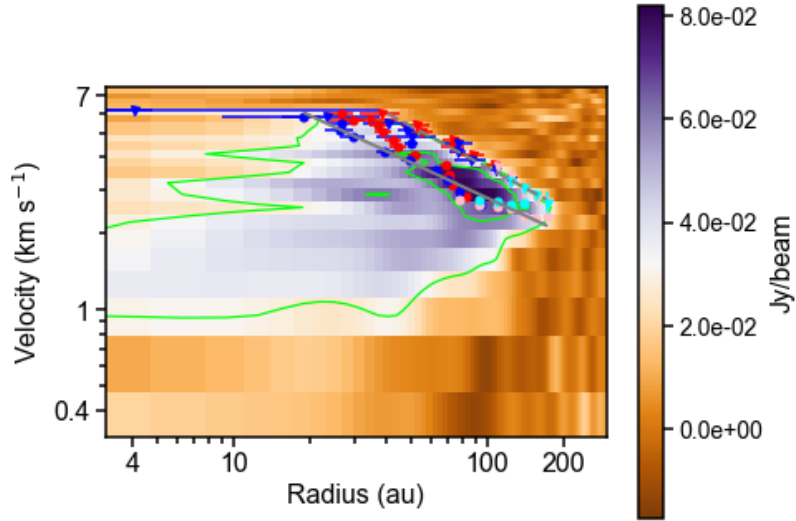


**Figure 13.** Folded and logarithmic PV diagram showing the position of the point found by SLAM in Band 7 spw 3

Gregorio-Hetem, J., Lepine, J. R. D., Quast, G. R., Torres, C. A. O., & de La Reza, R. 1992, AJ, 103, 549, doi: [10.1086/116082](https://doi.org/10.1086/116082)

Harris, C. R., Millman, K. J., van der Walt, S. J., et al. 2020, Nature, 585, 357, doi: [10.1038/s41586-020-2649-2](https://doi.org/10.1038/s41586-020-2649-2)

Huang, J., Andrews, S. M., Dullemond, C. P., et al. 2018a, ApJL, 869, L42, doi: [10.3847/2041-8213/aaf740](https://doi.org/10.3847/2041-8213/aaf740)

Huang, J., Andrews, S. M., Pérez, L. M., et al. 2018b, ApJL, 869, L43, doi: [10.3847/2041-8213/aaf7a0](https://doi.org/10.3847/2041-8213/aaf7a0)

Hunter, J. D. 2007, Computing in Science & Engineering, 9, 90, doi: [10.1109/MCSE.2007.55](https://doi.org/10.1109/MCSE.2007.55)

Isella, A. 2006, PhD thesis, Universita degli Studi di Milano, Milano, Italy

- Jennings, J., Booth, R. A., Tazzari, M., Rosotti, G. P., & Clarke, C. J. 2020, MNRAS, 495, 3209, doi: [10.1093/mnras/staa1365](https://doi.org/10.1093/mnras/staa1365)
- Long, F., Andrews, S. M., Rosotti, G., et al. 2022, ApJ, 931, 6, doi: [10.3847/1538-4357/ac634e](https://doi.org/10.3847/1538-4357/ac634e)
- Pedregosa, F., Varoquaux, G., Gramfort, A., et al. 2011, Journal of Machine Learning Research, 12, 2825
- Romero, G. A., Schreiber, M. R., Cieza, L. A., et al. 2012, ApJ, 749, 79, doi: [10.1088/0004-637X/749/1/79](https://doi.org/10.1088/0004-637X/749/1/79)
- Tazzari, M. 2017, mtazzari/uvplot, Zenodo, doi: [10.5281/zenodo.1003113](https://doi.org/10.5281/zenodo.1003113)
- Teague, R., & Foreman-Mackey, D. 2018, Research Notes of the American Astronomical Society, 2, 173, doi: [10.3847/2515-5172/aae265](https://doi.org/10.3847/2515-5172/aae265)
- Williams, J. P., & Cieza, L. A. 2011, ARA&A, 49, 67, doi: [10.1146/annurev-astro-081710-102548](https://doi.org/10.1146/annurev-astro-081710-102548)